

Fast rotating neutron stars with realistic nuclear matter equation of stateF. Cipolletta,^{1,*} C. Cherubini,^{2,3,†} S. Filippi,^{2,3,‡} J. A. Rueda,^{1,4,5,§} and R. Ruffini^{1,4,5,||}¹*Dipartimento di Fisica and International Center for Relativistic Astrophysics-ICRA,
Sapienza Università di Roma, P.le Aldo Moro 5, I-00185 Rome, Italy*²*Nonlinear Physics and Mathematical Modeling Lab, University Campus Bio-Medico of Rome,
Via A. del Portillo 21, I-00128 Rome, Italy*³*International Center for Relativistic Astrophysics-ICRA, University Campus Bio-Medico of Rome,
Via A. del Portillo 21, I-00128 Rome, Italy*⁴*International Center for Relativistic Astrophysics Network-ICRANet, Piazza della Repubblica 10,
I-65122 Pescara, Italy*⁵*International Center for Relativistic Astrophysics Network-ICRANet-Rio, Centro Brasileiro de
Pesquisas Físicas, Rua Dr. Xavier Sigaud 150, Rio de Janeiro 22290-180, Brazil*

(Received 19 February 2015; published 13 July 2015)

We construct equilibrium configurations of uniformly rotating neutron stars for selected relativistic mean-field nuclear matter equations of state (EOS). We compute, in particular, the gravitational mass (M), equatorial (R_{eq}) and polar (R_{pol}) radii, eccentricity, angular momentum (J), moment of inertia (I) and quadrupole moment (M_2) of neutron stars stable against mass shedding and secular axisymmetric instability. By constructing the constant frequency sequence $f = 716$ Hz of the fastest observed pulsar, PSR J1748–2446ad, and constraining it to be within the stability region, we obtain a lower mass bound for the pulsar, $M_{\text{min}} = [1.2\text{--}1.4]M_{\odot}$, for the EOS employed. Moreover, we give a fitting formula relating the baryonic mass (M_b) and gravitational mass of nonrotating neutron stars, $M_b/M_{\odot} = M/M_{\odot} + (13/200)(M/M_{\odot})^2$ [or $M/M_{\odot} = M_b/M_{\odot} - (1/20)(M_b/M_{\odot})^2$], which is independent of the EOS. We also obtain a fitting formula, although not EOS independent, relating the gravitational mass and the angular momentum of neutron stars along the secular axisymmetric instability line for each EOS. We compute the maximum value of the dimensionless angular momentum, $a/M \equiv cJ/(GM^2)$ (or “Kerr parameter”), $(a/M)_{\text{max}} \approx 0.7$, found to be also independent of the EOS. We then compare and contrast the quadrupole moment of rotating neutron stars with the one predicted by the Kerr exterior solution for the same values of mass and angular momentum. Finally, we show that, although the mass quadrupole moment of realistic neutron stars never reaches the Kerr value, the latter is closely approached from above at the maximum mass value, as physically expected from the no-hair theorem. In particular, the stiffer the EOS, the closer the mass quadrupole moment approaches the value of the Kerr solution.

DOI: [10.1103/PhysRevD.92.023007](https://doi.org/10.1103/PhysRevD.92.023007)

PACS numbers: 97.10.Kc, 04.25.D-, 04.40.Dg, 26.60.Kp

I. INTRODUCTION

Understanding the physics of neutron stars and being able to describe the spacetime in the interior and around such compact objects is one of the most important objectives for modern astrophysics, as from one side it could be an excellent test for general relativity and on the other the strong forces acting and the high level of densities reached cannot be tested anywhere on the Earth.

Although we are actually incapable of describing these concepts exactly, some observational limits have already been determined, via simplifying assumptions (such as a spherical configuration in the x-ray binaries observation). Other general considerations on the nature of neutron stars and pulsars are often extracted in the literature from the use

of fiducial structure parameters: a canonical neutron star (NS) of mass $M = 1.4M_{\odot}$, radius $R = 10$ km, and moment of inertia $I = 10^{45}$ g cm² (see, e.g., Ref. [1] and references therein). Based on these parameters together with the thus-inferred surface magnetic field from the classic pointlike magnetodipole rotating model [2,3], NSs have been traditionally classified according to the assumed nature of the energy source powering their observed emission. Neutron stars are also thought to possibly participate in the most powerful explosions in the Universe, gamma-ray bursts (GRBs), e.g., via NS mergers in the case of short GRBs (see, e.g., Ref. [4] and references therein) and hypercritical accretion processes leading to gravitational collapse to a black hole (BH) in the case of long GRBs associated with supernovae (see, e.g., Refs. [5,6] and references therein).

There are still, however, many open issues regarding the above global picture of NSs, both from the physics and the astrophysics points of view (see, e.g., Refs. [7,8]). On the other hand, our theoretical and observational knowledge on NSs has largely increased in the intervening years from the first general relativistic description of a NS by

*cipo87@gmail.com

†c.cherubini@unicampus.it

‡s.filippi@unicampus.it

§jorge.rueda@icra.it

||ruffini@icra.it

Oppenheimer and Volkoff in 1939 [9]. Eventually, a more complex equation of state (EOS), interior structure, and consequently exterior gravitational field of nonrotating, slowly rotating, and fast rotating stars were acquired, and massive NSs of $\approx 2M_\odot$, drastically constraining the nuclear EOS stiffness, were observed [10,11]. Thus, general conclusions based on fiducial parameters and corresponding observables might be premature, and a more exhausting exploration of the consequences of adopting different NS parameters appears to be necessary.

For instance, as recently shown in [12] for the high-magnetic field pulsar class, thought to be intermediate objects linking pulsars and magnetars, for the understanding of their magnetic field values and their energy source, we need precise knowledge of the entire set of possible structure parameters of a NS and a self-consistent general relativistic description of the pulsar observables. Indeed, it was shown there how the magnetic field of a pulsar is overestimated, and how the rotational energy is underestimated, by the classic magnetic rotating dipole model and the use of fiducial NS parameters.

The description of the rotational and thermal evolution, as well as the emitted radiation of isolated and accreting NS, requires knowledge of the structure properties and the corresponding exterior metric. For instance, we have recently compared and contrasted the cooling evolution of neutral NSs satisfying local charge neutrality and global charge neutrality [13]. In that work we have shown that, owing to their different crust structure (mass and thickness) for the same value of the total mass, their thermal relaxation time (the time to form an isothermal core) can be very different, and therefore, the signatures of the structure of the NS might be accessed via early cooling observations.

There have been recent numerical relativity computations of the structure of uniformly rotating NSs which have mainly focused on the existence of universal relations between, e.g., the quadrupole moment, the moment of inertia, and the Love number of NSs (see, e.g., Refs. [14–17]), considered in a slow rotation regime. Other works (e.g., Refs. [18,19]) also tried to recover these relations in a full rotation regime, with a numerical method based on the one first implemented in [20].

In this work, through a full rotation approach (treated by numerical relativity methods), we focus on additional structure properties of uniformly rotating NSs relevant for astrophysical applications such as mass, polar and equatorial radii, eccentricity, angular momentum, angular velocity, moment of inertia, and quadrupole moment, for a selected sample of EOS (describing nuclear matter with relations of different stiffness) within relativistic mean-field nuclear theory, not analyzed in the set of EOS of previous works.

This article is organized as follows. In Sec. II we briefly review the axisymmetric system of Einstein's equations to be integrated for a given EOS which we describe in Sec. III. The stability conditions (mass-shedding and secular instability) are outlined in Sec. IV, and the mass radius of

rotating NSs is shown in Sec. V. The eccentricity and the moment of inertia are shown in Sec. VI, while the quadrupole moment is discussed in Sec. VII. We finally summarize and discuss our results in Sec. VIII.

II. STRUCTURE EQUATIONS

We consider the equilibrium equations for a self-gravitating, rapidly rotating NS, within a fully general relativistic framework. We start with the stationary axisymmetric spacetime metric (see, e.g., Ref. [21]):

$$ds^2 = -e^{2\nu} dt^2 + e^{2\psi} (d\phi - \omega dt)^2 + e^{2\lambda} (dr^2 + r^2 d\theta^2), \quad (1)$$

where ν , ψ , ω and λ depend only on variables r and θ . It is useful to introduce the variable $e^\psi = r \sin(\theta) B e^{-\nu}$, with again $B = B(r, \theta)$. The above form of the metric is obtained under two assumptions: (1) there are two Killing vector fields, one timelike, t^a , and one relative to the axial symmetry, ϕ^a ; (2) the spacetime is asymptotically flat. Then, one can introduce quasi-isotropic coordinates, which in the nonrotating limit tend to isotropic ones.

Turning to the physical matter content in the NS interior, if one neglects sources of nonisotropic stresses, viscosity, and heat transport, then the energy-momentum tensor becomes one of a perfect fluid,

$$T^{\alpha\beta} = (\varepsilon + P) u^\alpha u^\beta + P g^{\alpha\beta}, \quad (2)$$

where ε and P denote the energy density and pressure of the fluid, and u^α is the fluid 4-velocity. In terms of the two Killing vectors,

$$u^\alpha = \frac{e^{-\nu} (t^\alpha + \Omega \phi^\alpha)}{\sqrt{1 - v^2}}, \quad (3)$$

where v is the fluid 3-velocity with respect to the local zero angular-momentum observer (ZAMO),

$$v = (\Omega - \omega) e^{\psi - \nu} \quad (4)$$

with $\Omega \equiv u^\phi / u^t = d\phi / dt$ the angular velocity in the coordinate frame, equivalent to the one measured by an observer at rest at infinity.

Thus, with the metric given by Eq. (1) and the energy-momentum tensor given by Eq. (2), one can write the field equations as (analogously to Ref. [22] setting $\zeta = \lambda + \nu$)

$$\begin{aligned} \nabla \cdot (B \nabla \nu) &= \frac{1}{2} r^2 \sin^2 \theta B^3 e^{-4\nu} \nabla \omega \cdot \nabla \omega \\ &+ 4\pi B e^{2\zeta - 2\nu} \left[\frac{(\varepsilon + P)(1 + v^2)}{1 - v^2} + 2P \right], \end{aligned} \quad (5)$$

$$\nabla \cdot (r^2 \sin^2 \theta B^3 e^{-4\nu} \nabla \omega) = -16\pi r \sin \theta B^2 e^{2\zeta-4\nu} \frac{(\varepsilon + P)v}{1-v^2}, \quad (6)$$

$$\nabla \cdot (r \sin(\theta) \nabla B) = 16\pi r \sin \theta B e^{2\zeta-2\nu} P, \quad (7)$$

$$\begin{aligned} \zeta_{,\mu} = & - \left\{ (1-\mu^2) \left(1 + r \frac{B_r}{B} \right)^2 + \left[\mu - (1-\mu^2) \frac{B_r}{B} \right]^2 \right\}^{-1} \left[\frac{1}{2} B^{-1} \{ r^2 B_{,rr} - [(1-\mu^2) B_{,\mu}]_{,\mu} - 2\mu B_{,\mu} \} \right. \\ & \times \left\{ -\mu + (1-\mu^2) \frac{B_{,\mu}}{B} \right\} + r \frac{B_r}{B} \left[\frac{1}{2} \mu + \mu r \frac{B_r}{B} + \frac{1}{2} (1-\mu^2) \frac{B_{,\mu}}{B} \right] + \frac{3}{2} \frac{B_{,\mu}}{B} \left[-\mu^2 + \mu(1-\mu^2) \frac{B_{,\mu}}{B} \right] \\ & - (1-\mu^2) r \frac{B_{,\mu r}}{B} \left(1 + r \frac{B_r}{B} \right) - \mu r^2 (\nu_{,r})^2 - 2(1-\mu^2) r \nu_{,\mu} \nu_{,r} + \mu(1-\mu^2) (\nu_{,\mu})^2 - 2(1-\mu^2) r^2 B^{-1} B_{,r} \nu_{,\mu} \nu_{,r} \\ & + (1-\mu^2) B^{-1} B_{,\mu} [r^2 (\nu_{,r})^2 - (1-\mu^2) (\nu_{,\mu})^2] + (1-\mu^2) B^2 e^{-4\nu} \left\{ \frac{1}{4} \mu r^4 (\omega_{,r})^2 + \frac{1}{2} (1-\mu^2) r^3 \omega_{,\mu} \omega_{,r} \right. \\ & \left. \left. - \frac{1}{4} \mu (1-\mu^2) r^2 (\omega_{,\mu})^2 + \frac{1}{2} (1-\mu^2) r^4 B^{-1} B_{,r} \omega_{,\mu} \omega_{,r} - \frac{1}{4} (1-\mu^2) r^2 B^{-1} B_{,\mu} [r^2 (\omega_{,r})^2 - (-\mu^2) (\omega_{,\mu})^2] \right\} \right], \quad (8) \end{aligned}$$

where, in the equation for $\zeta_{,\mu}$, we introduced $\mu \equiv \cos(\theta)$.

The projection of the conservation of the energy-momentum tensor, normal to the 4-velocity, $(\delta_b^c + u^c u_b) \nabla_a T^{ab} = 0$, leads to the hydrostationary equilibrium equation:

$$P_{,i} + (\varepsilon + P) \left[\nu_{,i} + \frac{1}{1-v^2} \left(-v v_{,i} + v^2 \frac{\Omega_{,i}}{\Omega - \omega} \right) \right] = 0, \quad (9)$$

where $i = 1, 2, 3$ and, as usual, $A_{,i} \equiv \partial A / \partial x^i$.

For a barotropic EOS, $P = P(\varepsilon)$, and in the case of uniform rotation which we adopt in this work, the above hydrostationary equilibrium equation has a first integral that can be written as

$$\int_0^P \frac{dP}{\varepsilon + P} - \ln(u^a \nabla_a t) = \nu|_{\text{pole}}, \quad (10)$$

where the constant of motion has been obtained, for instance, at the pole of the star (see, e.g., Ref. [21]).

III. EQUATION OF STATE

To obtain a solution to the field equations, the matter EOS must be supplied. In general, a NS is composed of two regions, namely, the core and the crust. The core, with densities overcoming the nuclear saturation value, $\rho_{\text{nuc}} \approx 3 \times 10^{14} \text{ g cm}^{-3}$, is composed of a degenerate gas of baryons (e.g., neutrons, protons, hyperons) and leptons (e.g., electrons and muons). The crust, in its outer region ($\rho \leq \rho_{\text{drip}} \approx 4.3 \times 10^{11} \text{ g cm}^{-3}$), is composed of ions and electrons, while in its inner region ($\rho_{\text{drip}} < \rho < \rho_{\text{nuc}}$), there is an additional component of free neutrons dripped out from nuclei. For the crust, we adopt the Baym-Pethick-Sutherland

(BPS) EOS [23]. For the core, here we adopt modern models based on relativistic mean-field (RMF) theory. Indeed, RMF models have become the most used ones in NS literature; with their success mainly owing to important properties such as Lorentz covariance, intrinsic inclusion of spin, a simple mechanism of saturation for nuclear matter, and being consistently relativistic, they do not violate causality (see, e.g., Ref. [24]). We adopt, as is now becoming traditional, an extension of the original formulation of Boguta and Bodmer [25] in which nucleons interact via massive meson mediators of different nature providing the attractive long range (scalar σ) and repulsive short range (vector ω) of the nuclear force, isospin and surface effects (vector ρ). Meson-meson interactions can also be present; for instance, in the version of Boguta and Bodmer [25] a self-interacting scalar field potential is present in the form of a quartic polynomial with adjustable coefficients. Here we consider the possibility of including, in addition to such a potential, vector-vector interactions of the ω meson. For a very recent and comprehensive analysis of the performance of several RMF models in the description of observed properties of ordinary nuclei, we refer the reader to Ref. [26], and for a brief historical and chronological reconstruction of the developments of the RMF models, see Ref. [27].

Thus, we constrain ourselves to models in which the energy density and pressure are given by (in units with $\hbar = c = 1$) [26]

$$\begin{aligned} \varepsilon = & \frac{1}{2} m_\sigma^2 \sigma^2 + \frac{g_\sigma}{3} \sigma^3 + \frac{g_\sigma}{4} \sigma^4 - \frac{1}{2} m_\omega^2 \omega_0^2 - \frac{g_\omega}{4} (g_\omega^2 \omega_0^2)^2 \\ & - \frac{1}{2} m_\rho^2 \rho_0^2 + g_\omega \omega_0 n_B + \frac{g_\rho}{2} \rho_0 n_3 + \sum_{i=n,p,e,\mu} \varepsilon_i, \quad (11a) \end{aligned}$$

$$P = -\frac{1}{2}m_\sigma^2\sigma^2 - \frac{g_{\sigma 2}}{3}\sigma^3 - \frac{g_{\sigma 3}}{4}\sigma^4 + \frac{1}{2}m_\omega^2\omega_0^2 + \frac{g_{\omega 3}}{4}(g_\omega^2\omega_0^2)^2 + \frac{1}{2}m_\rho^2\rho_0^2 + \sum_{i=n,p,e,\mu} P_i, \quad (11b)$$

where $m_{\sigma,\omega,\rho}$ are the masses of the scalar and vector mesons, $g_{\sigma 2,3}$, g_ω , $g_{\omega 3}$ are coupling constants, σ denotes the scalar meson and ω_0 and ρ_0 , denote the time component of the ω and ρ vector mesons, respectively. The components ε_i and P_i for each kind of particle considered are

$$\varepsilon_{n,p} = \frac{2}{(2\pi)^3} \int_0^{k_{n,p}^F} \sqrt{k^2 + (m_{n,p}^*)^2} d^3k, \quad (12a)$$

$$\varepsilon_{e,\mu} = \frac{2}{(2\pi)^3} \int_0^{k_{e,\mu}^F} \sqrt{k^2 + (m_{e,\mu})^2} d^3k, \quad (12b)$$

$$P_{n,p} = \frac{1}{3} \frac{2}{(2\pi)^3} \int_0^{k_{n,p}^F} \frac{k^2}{\sqrt{k^2 + (m_{n,p}^*)^2}} d^3k, \quad (12c)$$

$$P_{e,\mu} = \frac{1}{3} \frac{2}{(2\pi)^3} \int_0^{k_{e,\mu}^F} \frac{k^2}{\sqrt{k^2 + (m_{e,\mu})^2}} d^3k, \quad (12d)$$

where m_i^* is the effective mass of baryons.

The scalar, isospin, and baryon densities are given, respectively, by

$$n_s = \frac{2}{(2\pi)^3} \sum_{i=n,p} \int_0^{k_i^F} \frac{m_i^*}{\sqrt{k^2 + (m_i^*)^2}} d^3k, \quad (13a)$$

$$n_3 = n_p - n_n, \quad (13b)$$

$$n_B = n_p + n_n, \quad (13c)$$

where $n_i = (k_i^F)^3/(3\pi^2)$ are the particle number densities, with k_i^F the particle Fermi momenta.

The equations of motion of the meson fields within the RMF approximation are

$$m_\sigma^2\sigma = g_\sigma n_s - g_{\sigma 2}\sigma^2 - g_{\sigma 3}\sigma^3, \quad (14a)$$

$$m_\omega^2\omega_0 = g_\omega n_B - g_{\omega 3}g_\omega(g_\omega\omega_0)^3, \quad (14b)$$

$$m_\rho^2\rho_0 = \frac{g_\rho}{2} n_3. \quad (14c)$$

A barotropic EOS can be obtained iff additional closure relations are supplied. The first condition to be imposed is the request of the stability of matter against beta decay. The second closure equation that has been traditionally adopted is the condition of local charge neutrality of the system. It has recently been shown that the latter condition is not fully consistent with the equilibrium equations in the presence of

multicomponent charged constituents such as protons and electrons (see [27] and references therein). Instead, one has to request only global charge neutrality. The new system of equations, referred to as Einstein-Maxwell-Thomas-Fermi (EMTF) equations, self-consistently introduce the Coulomb interactions in addition to the strong, weak, and gravitational interactions within a full general relativity framework. It is worth noting that in this case no perfectlike form of the total energy-momentum tensor is obtained since the presence of electromagnetic fields breaks the pressure isotropy. Static NSs fulfilling the EMTF equations were constructed in Ref. [27], and uniformly rotating configurations in the second-order Hartle approximation can be found in Ref. [28]. To construct rotating NSs beyond the slow rotation regime, we take advantage of existing public numerical codes (e.g., the RNS code; see Sec. V) that solve the field equations without any limitation of the rotation rate of the star. However, an implementation of the equations and boundary conditions of the EMTF system within these codes is not yet available. Thus, as a first step, we adopt the condition of local charge neutrality, bearing in mind the necessity of a future implementation of the EMTF equations of equilibrium in the fast rotation regime.

With both the beta equilibrium and the local charge neutrality conditions, a numerical relation between the energy density and the pressure can be obtained. Here we adopt the nuclear parametrizations (for the specific values of the coupling constants, particle, and meson field masses) NL3 [29], TM1 [30], and GM1 [31,32]. In Fig. 1, we compare and contrast the three selected EOS used in this work in the nuclear and supranuclear regimes, relevant for NS cores. In Sec. V, we show how this selection of EOSs is physically relevant, as well as from the astrophysical point of view.

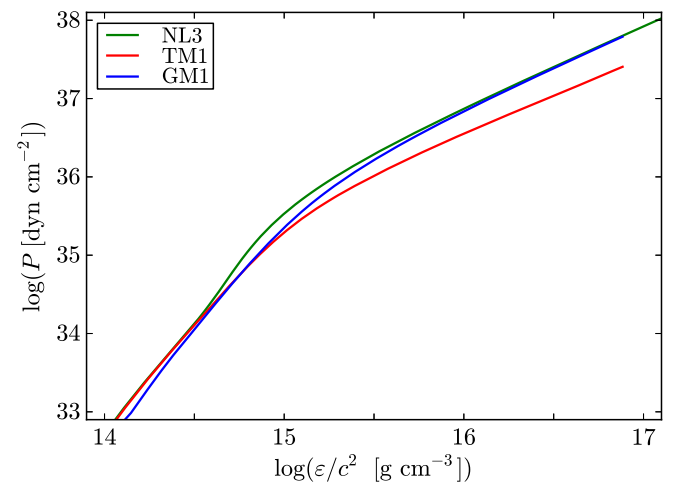


FIG. 1 (color online). Pressure-energy density relation for the three EOS (TM1, GM1, and NL3) used in the present article.

IV. STABILITY OF EQUILIBRIUM MODELS

To solve the system of field equations (5)–(8) and the hydrostationary equilibrium equation (10), one has to fix one (in the spherical static case) or two parameters (in the rotating case). The first quantity one has to fix is the central value of the energy density, ϵ_c . For a rotating model, one can choose the second parameter among different possibilities: the axes ratio ($r_{\text{pol}}/r_{\text{eq}}$) of coordinate radii, angular velocity (Ω), dimensionless angular momentum (j), gravitational mass (M), or baryonic mass (M_b). Thus, it is always possible to construct a sequence of rotating models by fixing a value of the second parameter and letting the central energy density vary in a given range which is constrained to stability limits that we now discuss.

The first limit on the stability of uniformly rotating configurations which we take into account is given by the sequence of maximally rotating stars, also referred to as the Keplerian or mass-shedding sequence. In all the stars belonging to such a sequence, the gravitational force equals the centrifugal force at the star equator, in such a way that faster rotation rates would induce the expulsion of mass from the star. The RNS code calculates this sequence by decreasing the axis ratio (which corresponds to an increase in angular velocity) until the angular velocity equals the one of a particle orbiting the star at its equator.

Another limit to the physically relevant models is determined by the so-called secular axisymmetric instability. For static configurations, the maximum stable mass (the critical mass) coincides with the first maximum of a sequence of configurations with increasing central density, namely, the first point where $\partial M/\partial \epsilon_c = 0$, with M the mass of a configuration with central density ϵ_c . At this point, the frequency of the radial perturbations vanishes. For higher densities, imaginary frequencies are obtained which lead to nonoscillatory perturbations, hence an instability. Thus, for static configurations, a turning point of the $M - \epsilon_c$ relation locates the onset of unstable configurations. This instability proceeds on secular timescales, i.e., not dynamical, so that it proceeds for long times, allowing the star to accommodate itself to the energy loss that occurs when going from one equilibrium point to another during gravitational collapse (see, e.g., Ref. [33] and references therein). As shown by Friedman, Ipser, and Sorkin in [33], the turning-point method leading to points of secular instability can also be used in uniformly rotating stars as follows. In a constant angular-momentum sequence, the turning point of a sequence of configurations with increasing central density separates secularly stable from secularly unstable configurations. Namely, secular axisymmetric instability sets in at

$$\left. \frac{\partial M(\epsilon_c, J)}{\partial \epsilon_c} \right|_{J=\text{constant}} = 0, \quad (15)$$

and therefore, the curve connecting all the maxima (turning points) limits the stability region. The intersection of such a limiting curve with the Keplerian sequence gives the fastest

possible configuration. It is important to mention that the numerical code adopted (described in the next section) builds sequences of constant dimensionless angular momentum, defined as

$$j \equiv \frac{cJ}{GM_\odot^2}, \quad (16)$$

which is the quantity we refer to in the sequel.

The angular momentum J is computed from the definition

$$J = \int_\Sigma T_{ab} \phi^a \hat{n}^b dV, \quad (17)$$

with Σ a spacelike 3-surface, $\hat{n}^a = \nabla_a t / |\nabla_b t \nabla^b t|$ the unit normal vector field to the t -constant spacelike hypersurfaces, and $dV = \sqrt{|^3g|} d^3x$ the proper 3-volume element (with 3g the determinant of the 3-metric). With this, Eq. (17) becomes [22]

$$J = \int B^2 e^{2\zeta - 4\nu} \frac{(\epsilon + P)v}{1 - v^2} r^3 \sin^2(\theta) dr d\theta d\phi. \quad (18)$$

V. MASS-RADIUS RELATION, OBSERVATIONAL CONSTRAINTS, AND STABILITY REGION

In the literature there are many different numerical schemes and, consequently, codes to compute relativistic, rotating figures of equilibrium. For the numerical integration of the equilibrium equations, in this work we use the public code RNS [34] by Stergioulas and Friedman [35]. This code is a numerical implementation based on the scheme by Cook, Shapiro, and Teukolsky [36] (first implemented for realistic NS EOS in [20]), which is a modified version of the method envisaged by Komatsu, Eriguchi, and Hachisu [37]. We refer the reader to Ref. [21] for further details on the numerical schemes.

The major intuitive effect of rotation is to deform the figure of equilibrium with respect to the spherical static counterpart. This can be seen from many points of view. For instance, we can compute sequences of constant angular velocity Ω . An important aspect should be taken into account however: the RNS code builds fast rotating models starting from a spherical (static) guess and decreases the polar to an equatorial radii ratio until the fixed parameter (e.g., the angular velocity) is reached with a prescribed accuracy. Thus, the axes ratio is a parameter used intrinsically by the numerical method, while other parameters (see the beginning of the previous section for a list) can be chosen but are reached by spanning decreasing values of the axis ratio. In particular, as an example, the code does not converge for every value of fixed angular velocity in every range of central energy density, and the range of convergence is reduced by decreasing the angular velocity. To be more precise, choosing fixed rotation frequencies below 300 Hz, the code fails to converge in the entire range in which equilibrium models should exist

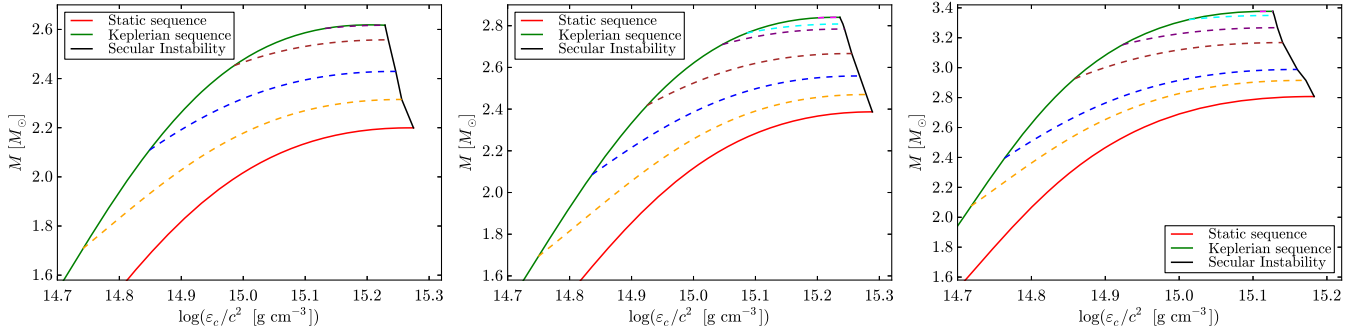


FIG. 2 (color online). Gravitational mass is plotted against central energy density for j -constant sequences obtained with the EOS TM1, GM1, and NL3 (from top to bottom). In this plot and hereafter, the red, green, and black curves represent, respectively, the static sequence, the Keplerian sequence, and the limit for secular stability. Here, other colors stand for various j -constant sequences.

(thus between the Keplerian and secular instability limits), even adopting a very dense numerical grid (300 angular times 600 radial points), different accuracy and tolerance values (down to 10^{-16}), or values of a relaxation factor from 1 to 0.8. Effectively, the code does converge for this kind of rotation frequency, but in very limited ranges of energy density. Thus, how can the slow rotation regime be recovered for every meaningful density? As technical advice, we mention that one could first compute sequences keeping various values of the axes ratio constant (in the vicinity of unity) and then select, in this set of models, the ones with small values of a particular angular velocity. With this simple method we construct the sequences with low rotation frequency (e.g., models from 50 Hz to 200 Hz). For other values of rotation frequency and for all other constant parameter sequences, we achieved optimal convergence using a 300 angular times 600 radial points numerical grid, and accuracy and tolerance of 10^{-8} , while the relaxation parameter was not necessary.

Figure 2 shows the total mass-central energy density plane for the selected EOS TM1, GM1, and NL3. We also show the stability limits discussed above in Sec. IV and show explicitly some constant angular-momentum sequences.

Figure 3 shows instead the total mass-central energy density plane, but in this case, we show explicitly some selected constant rotation frequency sequences ranging from 50 Hz all the way up to the rotation frequency of the fastest observed pulsar, PSR J1748–2446ad, with $f = \Omega/(2\pi) \approx 716$ Hz [38].

In Fig. 4 we plot the same Ω -constant sequences to show the relation between M and the equatorial radius, R_{eq} .

With the knowledge of the mass-radius relations predicted by the theory, we are now in a position to compare and contrast them with existing observational constraints, in order to validate the selection of EOS of the present work, not only from the already-presented physical aspects, but also from the astrophysical ones. Current observational constraints on the mass-radius relation of NSs are as follows (see Fig. 5):

- (i) *Most massive NS observed.*—The mass value of the most massive NS observed is the one of PSR

J1614–2230 with $2.01 \pm 0.04 M_{\odot}$ [39]. The rotation frequency of this pulsar is 46 Hz; thus, the deviations from spherical symmetry are negligible. This implies that every mass-radius relation for nonrotating NSs must have a maximum stable mass larger than this value.

- (ii) *Fastest observed NS.*—The highest rotation frequency observed in a pulsar is the one from PSR J1748–2446ad with $f = 716$ Hz [38]. The constant frequency sequence of this value for any mass-radius relation must have at least one stable configuration that supports such a rotation frequency; namely, the constant frequency sequence for this pulsar must lie within the region of stability. This is actually a very weak constraint since most NS models allow much higher rotation frequencies. Interestingly, as we show below, the construction of the constant frequency sequence for PSR J1748–2446ad allows us to infer a lower mass for this pulsar.
- (iii) *Constraints on the NS radius.*—Since the surface temperatures of not-so-young NSs ($t > 10^3$ – 10^4 y) are of the order of a million degrees (see, e.g., Ref. [13]), their thermal spectrum is expected to peak in the soft x rays. Thus, the modeling of the NS x-ray emission appears to be, at present, one of the most promising methods to obtain information on the NS radius. Systems that are currently used to this aim are isolated NSs, quiescent low-mass x-ray binaries (qLMXBs), NS bursters, and rotation-powered millisecond pulsars (see Ref. [40] and references therein). From the modeling of the observed spectrum, the radius of the NS as measured by an observer at infinity, $R_{\infty} = R/\sqrt{1 - 2GM/(c^2 R)}$, can be extracted.¹ The observation of a preferable

¹Actually, accurate spectra modeling leads to preferable values for both mass and radius; however, for a simpler comparison between different results from different methods and for a simple test of the mass-radius relation, it is sufficient to plot the constraints obtained from the values of R_{∞} consistent with the data [41].

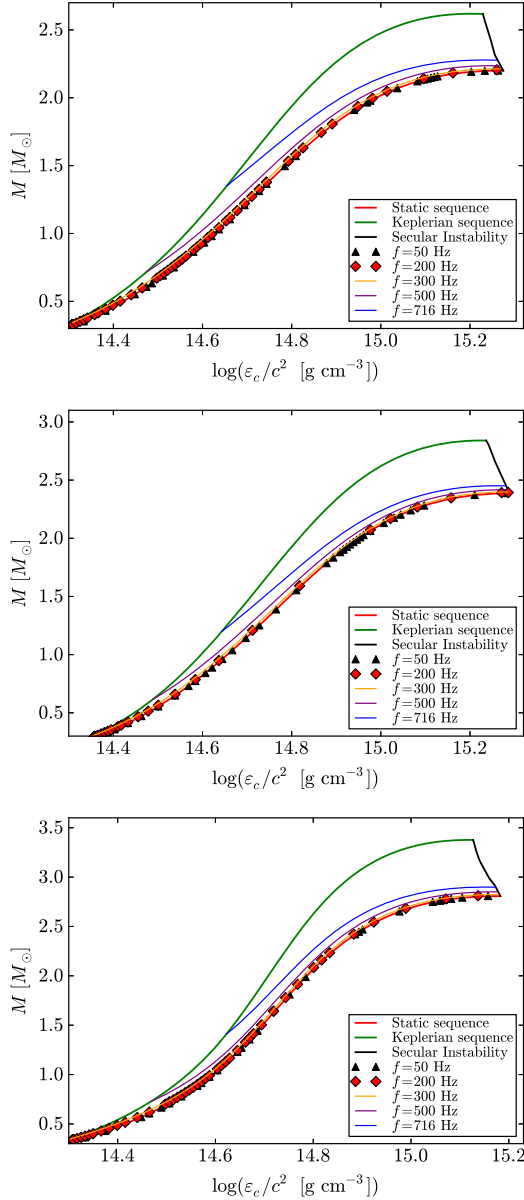


FIG. 3 (color online). Mass versus central energy density using the EOS TM1, GM1, and NL3 (from top to bottom) set of parameters. Red and green curves represent the static and Keplerian sequences. Other colors correspond to constant frequency sequences of values 716 Hz (fastest observed pulsar; blue), 500 Hz (purple), 300 Hz (orange), 200 Hz (red diamonds), and 50 Hz (black triangles).

radius at infinity clearly represents a constraint on the NS mass-radius relation since the above definition for R_∞ can be rewritten as $2GM/c^2 = R - R^3/(R_\infty^3)$. In Ref. [42] (see, also, Ref. [43]), the x-ray emission from the NSs in the qLMXBs M87, NGC 6397, M13, ω Cen, and NGC 6304 was revisited, and in Ref. [41] the one from the NS X7 in the Globular Cluster 47 Tucanae was examined. From the extracted values of R_∞ consistent with these observational data at 90% confidence level, we

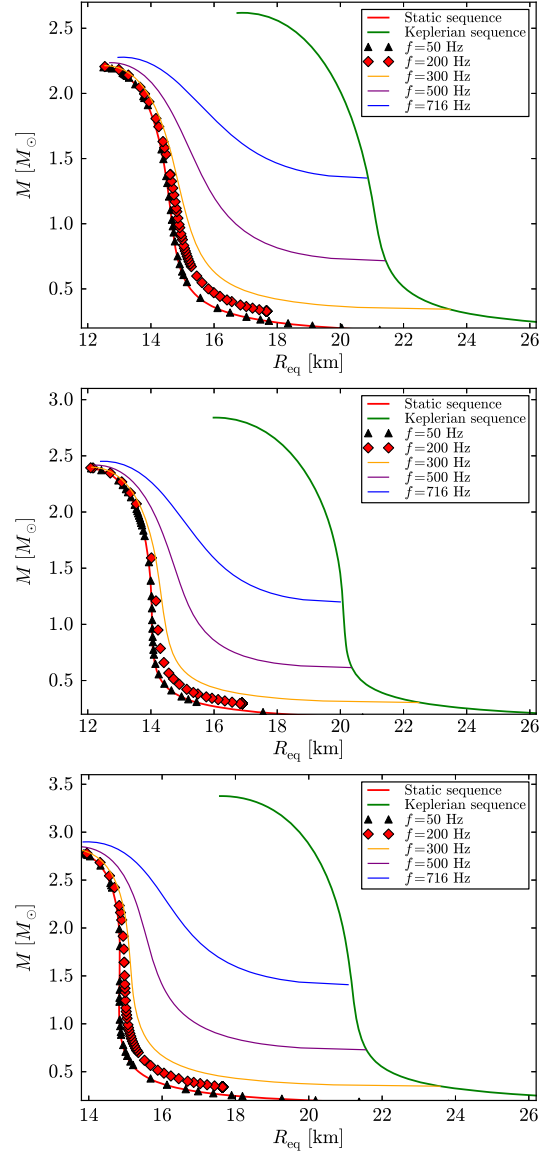


FIG. 4 (color online). Mass versus equatorial radius using the EOS TM1, GM1, and NL3 (from top to bottom) set of parameters for the same sequences as in Fig. 3. The convention of the plot colors and symbols is the same as in Fig. 3.

can conclude that the current x-ray data very weakly constrains the mass-radius relation, allowing radii in the interval $R_\infty = [7.64, 18.86]$, where the lower limit is obtained for NGC 6304 and the upper one for X7. It is important to mention that x-ray measurements suffer from a variety of uncertainties, which are the main reason for the very large spread in possible NS radii. The spectra modeling depends on the atmosphere composition, magnetic fields, accurate knowledge of the distance to the source, hence the extinction, and, to some extent, on the NS exterior geometry that could be affected by the rotation of the NS in the case of some LMXBs which could harbor NSs rotating with frequencies of

a few hundreds of Hz (see, e.g., Ref. [44] for details). In these latter cases, a more reliable comparison between theory and the above data constraints, which assume spherical symmetry, could be obtained by plotting the mass-radius relation using, instead of the equatorial radius, a mean or average spherical radius such as the authalic radius, $\langle R \rangle = (2R_{\text{eq}} + R_{\text{pol}})/3$. However, for the purposes of this work, it is sufficient to make a comparison with the mass-radius relation produced by the nonrotating configurations.

An additional constraint to the mass-radius relation might come from the request of causality to the EOS, namely, the condition that the speed of sound in the NS interior cannot exceed the speed of light. However, for the present set of EOS, this condition is automatically satisfied by construction since the models are relativistic. One can therefore see from Fig. 5 that the spherical (static) models (solid curves) obtained by the EOS selection of this work are in good agreement with the current constraints of the NS mass-radius relation determined by the most updated observational data.

An often useful physical quantity to be computed is the binding energy of the configurations, or the relation between the baryonic mass and the gravitational mass.

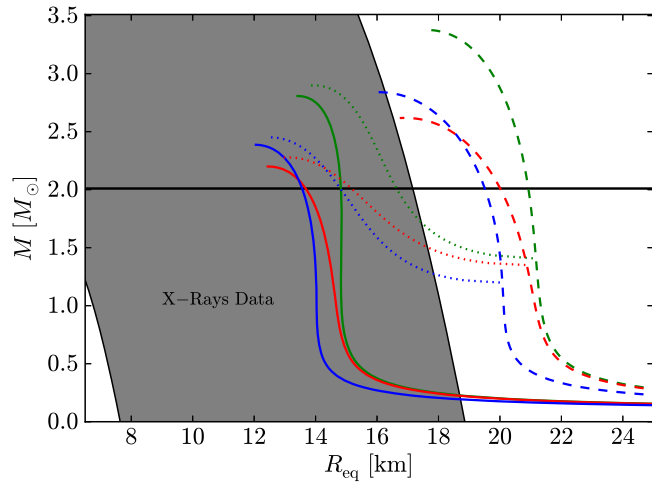


FIG. 5 (color online). Mass versus equatorial radius relation using the TM1, GM1, and NL3 EOS (red, blue, and green, respectively), plotted together with up-to-date observational constraints. Solid color curves represent static NS configurations; dotted color curves represent the sequence of models rotating with spin frequency of the fastest observed pulsar (PSR J1748–2446ad), $f = 716$ Hz; and dashed color curves represent sequences of models rotating at the Keplerian frequency. The gray-shaded region corresponds to the constraints given by the x-ray data, while the horizontal lines are the lower and upper bounds to the mass of the most massive observed pulsar, PSR J1614–2230, namely, $M = 2.01 \pm 0.04 M_{\odot}$. Further details of these constraints can be found in the text.

For nonrotating NSs, we found that for the three analyzed EOS, the following relations hold:

$$\begin{aligned} \frac{M_b}{M_{\odot}} &\approx \frac{M}{M_{\odot}} + \frac{13}{200} \left(\frac{M}{M_{\odot}} \right)^2, \\ \frac{M}{M_{\odot}} &\approx \frac{M_b}{M_{\odot}} - \frac{1}{20} \left(\frac{M_b}{M_{\odot}} \right)^2, \end{aligned} \quad (19)$$

where M_b is the baryonic mass. The apparent universality of these relations for the present set of EOS points to a universal behavior of the binding energy, namely independent of the EOS. The maximum relative errors obtained for nonrotating sequences of GM1, TM1, and NL3 are, respectively, 1.4%, 1.3%, and 0.99%. For rotating configurations, $M = M(M_b, J)$ or $M_b = M_b(M, J)$, we find that for our set of EOS, there is indeed a common relation given by

$$\frac{M_b}{M_{\odot}} = \frac{M}{M_{\odot}} + \frac{13}{200} \left(\frac{M}{M_{\odot}} \right)^2 \left(1 - \frac{1}{130} j^{1.7} \right), \quad (20)$$

which is accurate within an error of 2%, and which duly generalizes Eq. (19).

Turning back to the above plots, we can clearly see that, as expected, the higher the frequency of rotation, the higher the value of the mass at which the departures from the nonrotating mass-radius relation begin. We find that for rotation frequencies $\lesssim 200$ Hz (or rotation periods $\gtrsim 5$ ms), the nonrotating star becomes an accurate representation of the object. This is in accordance with previous results; see, e.g., Fig. 5 in Ref. [45], where it was shown that the moment of inertia of sequences computed with different EOS starts to deviate considerably from the static and the slow rotation Hartle’s approximations for frequencies above ~ 0.2 kHz. As we show below, this is also the case for the moment of inertia in the same range of frequencies (thus, the moment of inertia of nonrotating configurations can be safely approximated with the one of spinning configurations, with frequencies below the aforementioned limit, and vice versa). For higher frequencies, full rotation effects are needed for an accurate description. This is especially important for objects with masses lower than the maximum value, where departures from a nonrotating or slow rotation approximation become more and more evident.

Following this reasoning, it is important to see how a constant frequency sequence imposes structure constraints on a pulsar. Particularly interesting is the case of the $f = 716$ Hz sequence (blue curve), which corresponds to the fastest observed pulsar, PSR J1748–2446ad. The constant frequency sequence intersects the stability region in two points: at the maximally rotating Keplerian sequence, defining a minimum mass for the pulsar, and at the secular axisymmetric instability limit, in the upper part, defining the maximum possible mass for the given frequency. Clearly, these minimum and maximum mass values depend upon the EOS. For the EOS employed here, we can see that the mass

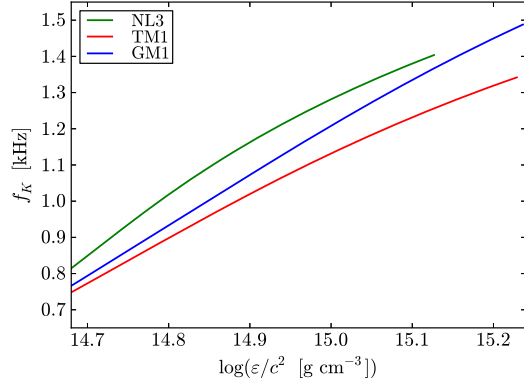


FIG. 6 (color online). Frequency of the maximally rotating configurations (Keplerian sequence) as a function of the total NS mass for the TM1, GM1, and NL3 EOS. The curves end at the maximum frequency configuration, which is located at the intersection between the Keplerian and the secular axisymmetric instability sequences.

of PSR J1748–2446ad has to be $\gtrsim [1.41, 1.35, 1.20]M_\odot$ for NL3, TM1, and GM1, respectively.

We now determine the maximum rotation frequency of NSs. The fastest configuration for a given EOS is the one that terminates the Keplerian sequence, namely, the configuration at the intersection between the Keplerian and the secular axisymmetric instability sequences. We show in Fig. 6 the rotation frequency of the maximally rotating configurations, i.e., the frequencies of the NSs along the Keplerian sequence.

Another important quantity for this discussion is the dimensionless angular momentum (“Kerr parameter”), $a/M \equiv cJ/(GM^2)$, which we show in Fig. 7 as a function

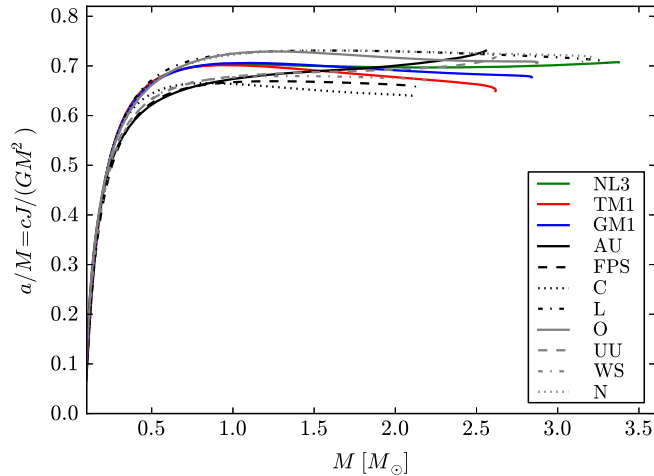


FIG. 7 (color online). Dimensionless angular momentum (“Kerr parameter”), $a/M \equiv cJ/(GM^2)$, as a function of the total NS mass along the Keplerian sequence for the EOS selected in this work (colored curves). For comparison, we show the results for additional EOS, taken from a set supplied by the RNS code (EOS.INDEX file). We refer the reader to the RNS web page and references therein for further details of these EOS.

of the total mass for the maximally rotating configurations, namely, the Keplerian sequence. It can be seen that the maximum value attained by the NS, $(a/M)_{\max} \approx 0.7$, holds for all the selected EOS. The maximum value is reached for the mass $[0.96, 1.05, 3.37]M_\odot$ for the TM1, GM1, and NL3 EOS, respectively. The existence of such a particular maximum (see, also [46]) EOS-independent, value of a possibly implies the existence of universal limiting values of the NS compactness and the rotational to gravitational energy ratio. This is a conjecture which deserves further exploration. In the same plot, the same sequences obtained with other already-known EOS (represented by differently dashed curves), assuming widely different kinds of interactions and via different many-body theories, are shown, and the reader can notice a general universal behavior of the dimensionless angular momentum, even if for these other EOS, the exact maximal values of this dimensionless parameter are slightly different. On the other hand, such a general behavior of the a parameter is not surprising in fact, as it was already shown in Ref. [19], it can be chosen as a parameter to establish a universal I-Love-Q relation. Nevertheless, the important argument here is that, although with different stiffness, our chosen set of EOS presents a common maximal dimensionless angular momentum a/M .

In Table I we summarize a few relevant quantities of NSs; the maximum stable mass in the nonrotating case, the maximum mass in the case of uniform rotation, the maximum rotation frequency, and the maximum value of the dimensionless angular momentum.

Before closing this section, we would like to provide a formula, useful for astrophysical applications, for the masses of the NSs lying along the secular axisymmetric instability line. Using the dimensionless angular momentum j , defined in Eq. (16) and related to the Kerr parameter by $j = (M/M_\odot)^2 a$, we obtain

$$M = M_{\max}^{J=0}(1 + kj^l), \quad (21)$$

where the values of $M_{\max}^{J=0}$ are given in Table I, $k = [0.017, 0.011, 0.0060]$ and $l = [1.61, 1.69, 1.68]$ for the EOS TM1, GM1, NL3, respectively. The maximum relative errors obtained for values of mass along the secular axisymmetric instability line with respect to fits for each EOS are, respectively, $[0.33\%, 0.44\%, 0.45\%]$.

TABLE I. Some properties of NSs for the selected EOS: critical mass for nonrotating case, $M_{\max}^{J=0}$; maximum mass in uniform rotation, $M_{\max}^{J \neq 0}$; maximum rotation frequency, f_{\max} ; and maximum dimensionless angular momentum (“Kerr parameter”), $(a/M)_{\max} \equiv [cJ/(GM^2)]_{\max}$.

EOS	$M_{\max}^{J=0} [M_\odot]$	$M_{\max}^{J \neq 0} [M_\odot]$	$f_{\max} [\text{kHz}]$	$(a/M)_{\max}$
TM1	2.20	2.62	1.34	0.70
GM1	2.39	2.84	1.49	0.71
NL3	2.81	3.38	1.40	0.71

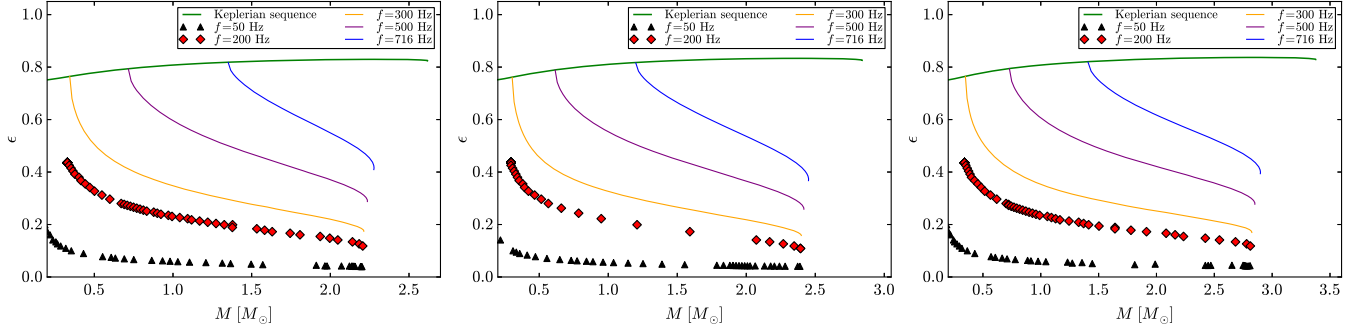


FIG. 8 (color online). Eccentricity versus gravitational mass using EOS with the TM1, GM1, and NL3 (from left to right) set of parameters for the same sequences as in Fig. 3.

VI. ECCENTRICITY AND MOMENT OF INERTIA

In order to see how a figure of equilibrium becomes deformed by rapid rotation, we compute the eccentricity

$$\epsilon = \sqrt{1 - \left(\frac{R_{\text{pol}}}{R_{\text{eq}}}\right)^2}, \quad (22)$$

which we plot in Fig. 8 as a function of the mass M for the same constant Ω sequences of the previous figures.

It is also interesting to investigate the distribution of the energy density within the figure of equilibrium for both the static and rotational cases for the different EOS. In Fig. 9 we show the contours of constant energy density of a model with central value $\epsilon_c = 10^{15} \text{ g cm}^{-3}$, both in the static case and in the rotational one with dimensionless angular momentum $j = 4$, for the sake of example, for the GM1 EOS.

We now compute the moment of inertia of the star, which is one of the most relevant properties in pulsar analysis. The moment of inertia can be estimated as [21]

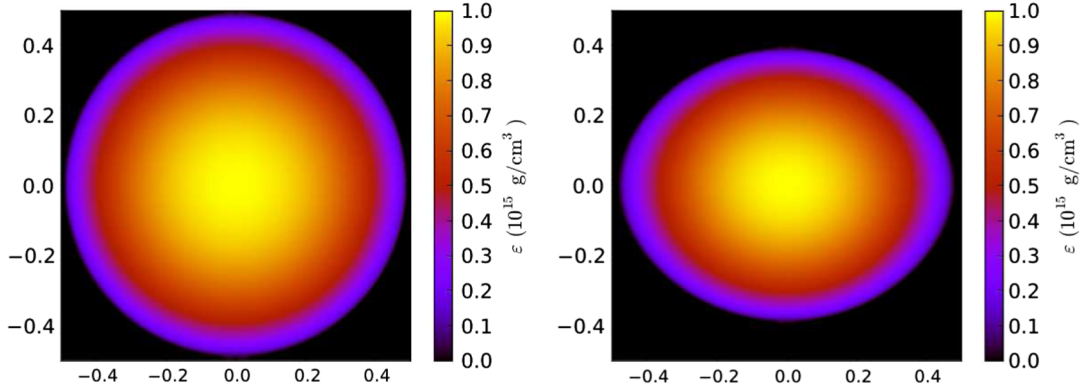


FIG. 9 (color online). Contours of constant energy density of a model with central value $\epsilon_c = 10^{15} \text{ g cm}^{-3}$, both in the static case (left plot) and in the rotational one with dimensionless angular momentum $j = 4$ (right plot) for the GM1 EOS.

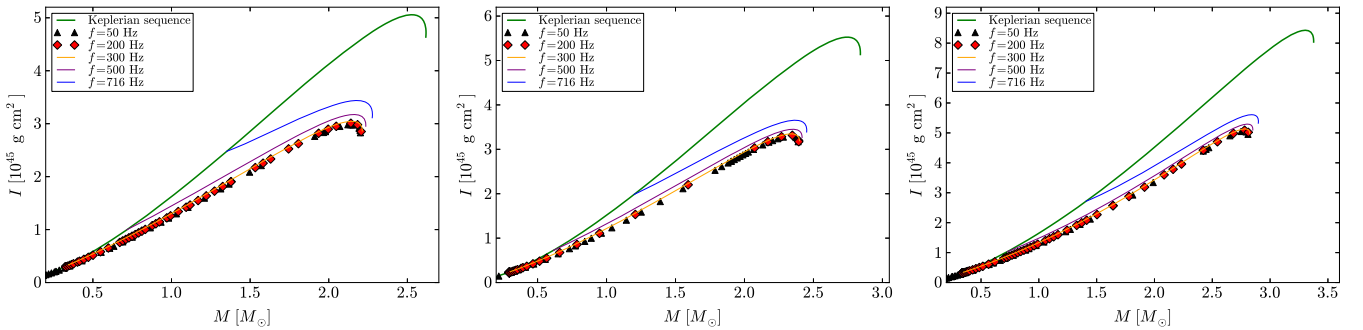


FIG. 10 (color online). Moment of inertia versus mass relation using the EOS TM1, GM1, and NL3 (from top to bottom) set of parameters for the same sequences as in Fig. 3.

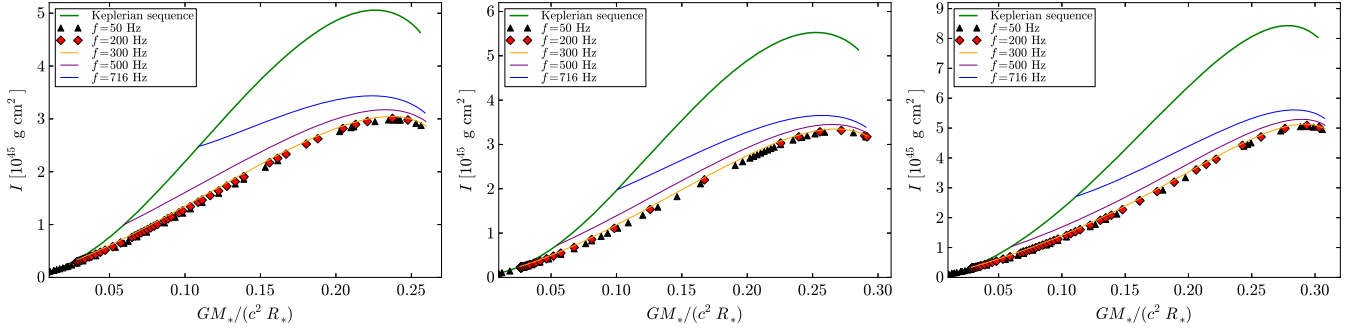


FIG. 11 (color online). Moment of inertia versus compactness using EOS with the TM1, GM1, and NL3 (from left to right) set of parameters for the same sequences as in Fig. 3.

$$I = \frac{J}{\Omega}, \quad (23)$$

where J is the star angular momentum which is given by Eq. (18).

In Fig. 10 we plot the moment of inertia as a function of the mass for some Ω -constant sequences together with the Keplerian sequence, while in Fig. 11 we show the relations between I and the compactness, $GM_*/(c^2 R_*)$, where M_* and R_* are the mass and the radius of the spherical configuration with the same central density as the rotating one, ε_c .

The above figures confirm that for rotation frequencies $\lesssim 200$ Hz, or rotation periods $\gtrsim 5$ ms, the deformation of the star is very small and, indeed, the nonrotating or the

slow rotation regimes can be safely adopted as accurate approximations of the rotating NS.

VII. QUADRUPOLE MOMENT

The quadrupole moment in the RNS code is given by

$$M_2 = \frac{1}{2} r_{\text{eq}}^3 \int_0^1 \frac{s'^2 ds'}{(1-s')^4} \int_0^1 P_2(\mu') \tilde{S}_\rho(s', \mu') d\mu', \quad (24)$$

where r_{eq} is the value of the coordinate radius at the equator, $\rho \equiv 2\nu - \ln(B)$, $s = r/(r + r_{\text{eq}}) \in [0, 1]$ is a compacted radial coordinate, $\mu = \cos(\theta)$, $P_2(\mu)$ is the Legendre polynomial of second order, and $\tilde{S}_\rho = r^2 S_\rho$, with S_ρ a source function defined as

$$S_\rho(r, \mu) = e^{\frac{1}{2}\gamma} \left[8\pi e^{2\lambda} (\varepsilon + P) \frac{1+u^2}{1-u^2} + r^2 e^{-2\rho} \left[\omega_{,r}^2 + \frac{1}{r^2} (1-\mu^2) \omega_{,\mu}^2 \right] + \frac{1}{r} \gamma_{,r} - \frac{1}{r^2} \mu \gamma_{,\mu} \right. \\ \left. + \frac{\rho}{2} \left\{ 16\pi e^{2\lambda} - \gamma_{,r} \left(\frac{1}{2} \gamma_{,r} + \frac{1}{r} \right) \frac{1}{r^2} \gamma_{,\mu} \left[\frac{1}{2} \gamma_{,\mu} (1-\mu^2) - \mu \right] \right\} \right], \quad (25)$$

with $\gamma = \ln(B)$. However, as shown in Ref. [14], Eq. (24) is not the actual quadrupole moment of the rotating source according to the Geroch-Hansen multipole moments [47–49]. Indeed, the quadrupole moment extracted via Ryan’s expansion method [50] is [14,15]

$$M_2^{\text{corr}} = M_2 - \frac{4}{3} \left(\frac{1}{4} + b_0 \right) M^3, \quad (26)$$

$$b_0 = -\frac{16\sqrt{2}\pi r_{\text{eq}}^4}{M^2} \int_0^{\frac{1}{2}} \frac{s'^3 ds'}{(1-s')^5} \\ \times \int_0^1 d\mu' \sqrt{1-\mu'^2} P(s', \mu') e^{\gamma+2\lambda} T_0^{\frac{1}{2}}(\mu'), \quad (27)$$

where M_2 is given by Eq. (24) and $T_0^{\frac{1}{2}}$ is the Gegenbauer polynomial of order 0 with normalization $T_0^{1/2} = \sqrt{2/\pi} C_0$, with C_0 the traditional 0th-order Gegenbauer polynomial.

Following Refs. [14,15], we numerically computed the correction factor b_0 given by Eq. (27), and then obtained the corrected quadrupole moment through Eq. (26). In Fig. 12 the modulus of M_2^{corr} is plotted in logarithmic scale against the gravitational mass for selected constant frequency sequences. Each sequence was stopped at the secular instability limit. We can see that the quadrupole moment is a decreasing function of the mass along a constant frequency sequence, while it is an increasing function along the Keplerian sequence.

We now compare and contrast the above mass quadrupole moment with the one from the Kerr solution,

$$M_2^{\text{Kerr}} = \frac{J^2}{M}. \quad (28)$$

The reason for this is twofold. First, we point out the long-discussed question in astrophysics of whether the Kerr

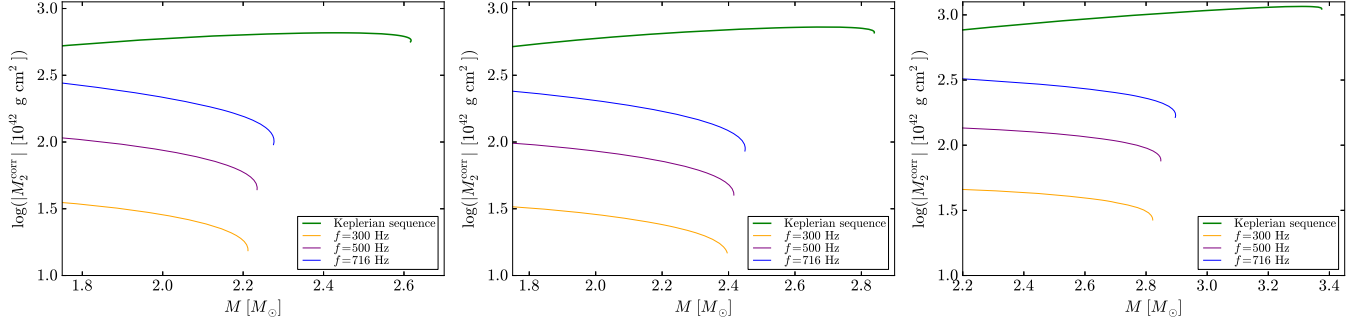


FIG. 12 (color online). The modulus of the corrected value for the mass quadrupole (in logarithmic scale) obtained via Eq. (26) is plotted against gravitational mass for the same constant frequency sequences of Fig. 3.

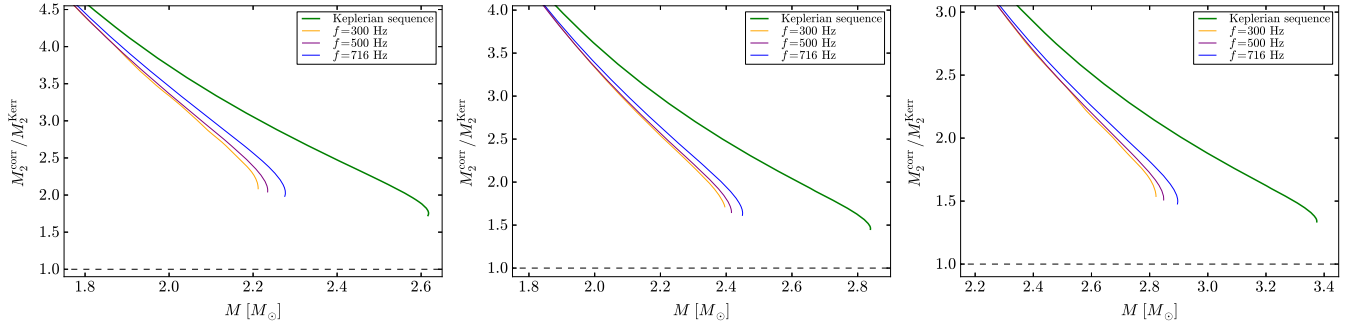


FIG. 13 (color online). $M_2^{\text{corr}}/M_2^{\text{Kerr}}$ ratio for the same selected sequences of constant frequency of Fig. 12 and EOS TM1, GM1, and NL3 (from left to right). We show here only the region of large masses where M_2^{corr} starts to approach the Kerr value M_2^{Kerr} .

solution may describe the exterior gravitational field of a realistic astrophysical source besides a black hole; namely, is there any matter content which could generate a Kerr exterior field? (See, e.g., Refs. [51,52] and references therein.) Second, if the answer to the previous question is negative, then one can distinguish a NS from a black hole with the same mass and angular momentum from the knowledge of the quadrupole moment (see, e.g., Ref. [53] and references therein).

In Fig. 13 we show the ratio between the NS quadrupole moment M_2^{corr} , given by Eq. (26), and the Kerr solution quadrupole moment M_2^{Kerr} , for selected constant frequency sequences. We find that M_2^{corr} starts to approach M_2^{Kerr} , as intuitively expected, for masses close to the maximum stable value. An interesting feature that we can see from Fig. 13 is that the stiffer the EOS the more the quadrupole moment approaches the Kerr value. This result is in good accordance with previous results that showed that the compactness of the star increases, and also the moment of inertia, Love numbers, and mass quadrupole approach the ones of a black hole, though they will never coincide (see, e.g., Ref. [17]). Moreover, we confirm, in the full rotation regime, the previous result obtained in the slow rotation Hartle approximation [54], that the ratio $M_2^{\text{corr}}/M_2^{\text{Kerr}}$ is a decreasing function of the NS mass, hence reaching its lowest value at the maximum mass

configuration. Indeed, as we can see from Fig. 13, the larger the maximum mass attained by a NS model, the more the NS quadrupole moment approaches the Kerr solution value, reaching even values < 1.5 for stiff EOS such as the NL3 model.

VIII. DISCUSSIONS AND CONCLUSIONS

We have computed uniformly rotating NSs for the selected relativistic mean-field nuclear matter model EOS (TM1, GM1, and NL3). Specifically, we have calculated their gravitational mass, equatorial and polar radii, eccentricity, angular momentum, moment of inertia, and quadrupole moment. We have established the region of stability against mass shedding and the secular axisymmetric instability. We have provided plots of all these physical quantities, e.g., as a function of the mass of the configurations. We have also constructed sequences of constant rotation frequency and approximately determined the rotation rate at which deviations of the structure parameters from the spherically symmetric (or slowly rotating) values start, obtaining $f \approx 200$ Hz, a value in agreement with previous works (see, e.g., Ref. [45]).

From the astrophysical point of view, we have obtained a lower bound for the mass of the fastest observed pulsar, PSR J1748–2446ad with $f = 716$ Hz, by constructing its

constant rotation frequency sequence and constraining it to be within the stability region: we obtained $M_{\min} = [1.2\text{--}1.4]M_{\odot}$, for the EOS used in this work, a prediction submitted for observational verification. We have also obtained a fitting formula relating the baryonic and gravitational mass of nonrotating NSs [see Eq. (19)], independent of the EOS. We have computed a formula for the masses of NSs on the secular instability line as a function of their angular momentum [see Eq. (21)]. We studied the Kerr parameter (dimensionless angular momentum) of NSs and found that it reaches a maximum value $(a/M)_{\max} \approx 0.7$, independent of the EOS. This result brings us to the important conclusion that the gravitational collapse of a uniformly rotating NS, constrained to mass-energy and angular-momentum conservation, cannot lead to a maximally rotating Kerr black hole, which, by definition, has $(a/M)_{\text{BH,max}} = 1$. We have also shown that the quadrupole moment of realistic NSs does not reach the Kerr value (for the same values of mass and angular momentum), but this is closely approached from above at the maximum mass value, in physical agreement with the no-hair theorem. We have also found that the stiffer the EOS, the more the Kerr solution is approached.

It is important to stress that the results shown in this work for some specific nuclear EOS likely will remain valid in the case of other different models, provided they are

consistent with current observational constraints, especially the mass of PSR J0348 + 0432, $M = 2.01 \pm 0.04M_{\odot}$ [11]. The existence of such a massive NS clearly favors stiff nuclear EOS, such as the ones obtained via RMF theory, which leads to a critical NS mass higher than this constraint.

To conclude, as already mentioned in Sec. III, we would like to note the importance of considering a global charge neutrality condition for the system, instead of a local one, which needs a new and more complete code to treat these kinds of problems, including the case of fast rotating strange quark stars with crust, which show similar features in the core-crust transition.

ACKNOWLEDGMENTS

C. C. and S. F. would like to acknowledge GNFM-INDAM and ICRANet for partial support. It is a pleasure to thank D. P. Menezes and R. C. R. de Lima for discussions on the equation of state of NSs and for supplying the EOS tables. J. A. R. acknowledges support from the International Cooperation Program CAPES-ICRANet financed by CAPES—Brazilian Federal Agency for Support and Evaluation of Graduate Education within the Ministry of Education of Brazil.

-
- [1] P. A. Caraveo, *Annu. Rev. Astron. Astrophys.* **52**, 211 (2014).
 - [2] F. Pacini, *Nature (London)* **216**, 567 (1967).
 - [3] T. Gold, *Nature (London)* **218**, 731 (1968).
 - [4] F. G. Oliveira, J. A. Rueda, and R. Ruffini, *Astrophys. J.* **787**, 150 (2014).
 - [5] J. A. Rueda and R. Ruffini, *Astrophys. J. Lett.* **758**, L7 (2012).
 - [6] C. L. Fryer, J. A. Rueda, and R. Ruffini, *Astrophys. J. Lett.* **793**, L36 (2014).
 - [7] A. K. Harding, *Front. Phys.* **8**, 679 (2013).
 - [8] T. M. Tauris, V. M. Kaspi, R. P. Breton, A. T. Deller, E. F. Keane, M. Kramer, D. R. Lorimer, M. A. McLaughlin, A. Possenti, P. S. Ray, B. W. Stappers, and P. Weltevrede, *Proc. Sci.*, AASKA14 (2015) 039.
 - [9] J. R. Oppenheimer and G. M. Volkoff, *Phys. Rev.* **55**, 374 (1939).
 - [10] J. Antoniadis, M. H. van Kerkwijk, D. Koester, P. C. C. Freire, N. Wex, T. M. Tauris, M. Kramer, and C. G. Bassa, *Mon. Not. Roy. Astron. Soc.* **423**, 3316 (2012).
 - [11] J. Antoniadis *et al.*, *Science* **340**, 1232232 (2013).
 - [12] R. Belvedere, J. A. Rueda, and R. Ruffini, *Astrophys. J.* **799**, 23 (2015).
 - [13] S. M. de Carvalho, R. Negreiros, J. A. Rueda, and R. Ruffini, *Phys. Rev. C* **90**, 055804 (2014).
 - [14] G. Pappas and T. A. Apostolatos, *Phys. Rev. Lett.* **108**, 231104 (2012).
 - [15] K. Yagi, K. Kyutoku, G. Pappas, N. Yunes, and T. A. Apostolatos, *Phys. Rev. D* **89**, 124013 (2014).
 - [16] K. Yagi and N. Yunes, *Science* **341**, 365 (2013).
 - [17] K. Yagi and N. Yunes, *Phys. Rev. D* **88**, 023009 (2013).
 - [18] D. D. Doneva, S. S. Yazadjiev, N. Stergioulas, and K. D. Kokkotas, *Astrophys. J. Lett.* **781**, L6 (2014).
 - [19] S. Chakrabarti, T. Delsate, N. Gürlebeck, and J. Steinhoff, *Phys. Rev. Lett.* **112**, 201102 (2014).
 - [20] G. B. Cook, S. L. Shapiro, and S. A. Teukolsky, *Astrophys. J.* **424**, 823 (1994).
 - [21] N. Stergioulas, *Living Rev. Relativity* **6**, 3 (2003).
 - [22] E. M. Butterworth and J. R. Ipser, *Astrophys. J.* **204**, 200 (1976).
 - [23] G. Baym, C. Pethick, and P. Sutherland, *Astrophys. J.* **170**, 299 (1971).
 - [24] J. A. Rueda, R. Ruffini, Y.-B. Wu, and S.-S. Xue, *Phys. Rev. C* **89**, 035804 (2014).
 - [25] J. Boguta and A. R. Bodmer, *Nucl. Phys.* **A292**, 413 (1977).
 - [26] M. Dutra, O. Lourenço, S. S. Avancini, B. V. Carlson, A. Delfino, D. P. Menezes, C. Providência, S. Typel, and J. R. Stone, *Phys. Rev. C* **90**, 055203 (2014).
 - [27] R. Belvedere, D. Pugliese, J. A. Rueda, R. Ruffini, and S.-S. Xue, *Nucl. Phys.* **A883**, 1 (2012).

- [28] R. Belvedere, K. Boshkayev, J. A. Rueda, and R. Ruffini, *Nucl. Phys.* **A921**, 33 (2014).
- [29] G. A. Lalazissis, J. König, and P. Ring, *Phys. Rev. C* **55**, 540 (1997).
- [30] Y. Sugahara and H. Toki, *Nucl. Phys.* **A579**, 557 (1994).
- [31] N. K. Glendenning and S. A. Moszkowski, *Phys. Rev. Lett.* **67**, 2414 (1991).
- [32] S. Pal, D. Bandyopadhyay, and W. Greiner, *Nucl. Phys.* **A674**, 553 (2000).
- [33] J. L. Friedman, J. R. Ipser, and R. D. Sorkin, *Astrophys. J.* **325**, 722 (1988).
- [34] <http://www.gravity.phys.uwm.edu/rms/>.
- [35] N. Stergioulas and J. L. Friedman, *Astrophys. J.* **444**, 306 (1995).
- [36] G. B. Cook, S. L. Shapiro, and S. A. Teukolsky, *Astrophys. J.* **398**, 203 (1992).
- [37] H. Komatsu, Y. Eriguchi, and I. Hachisu, *Mon. Not. Roy. Astron. Soc.* **237**, 355 (1989).
- [38] J. W. T. Hessels, S. M. Ransom, I. H. Stairs, P. C. C. Freire, V. M. Kaspi, and F. Camilo, *Science* **311**, 1901 (2006).
- [39] P. B. Demorest, T. Pennucci, S. M. Ransom, M. S. E. Roberts, and J. W. T. Hessels, *Nature (London)* **467**, 1081 (2010).
- [40] M. Fortin, J. L. Zdunik, P. Haensel, and M. Bejger, *Astron. Astrophys.* **576**, A68 (2015).
- [41] C. O. Heinke, G. B. Rybicki, R. Narayan, and J. E. Grindlay, *Astrophys. J.* **644**, 1090 (2006).
- [42] J. M. Lattimer and A. W. Steiner, *Eur. Phys. J. A* **50**, 40 (2014).
- [43] C. O. Heinke, H. N. Cohn, P. M. Lugger, N. A. Webb, W. C. G. Ho, J. Anderson, S. Campana, S. Bogdanov, D. Haggard, A. M. Cool, and J. E. Grindlay, *Mon. Not. Roy. Astron. Soc.* **444**, 443 (2014).
- [44] M. Bauböck, F. Özel, D. Psaltis, and S. M. Morsink, *Astrophys. J.* **799**, 22 (2015).
- [45] O. Benhar, V. Ferrari, L. Gualtieri, and S. Marassi, *Phys. Rev. D* **72**, 044028 (2005).
- [46] K.-W. Lo and L.-M. Lin, *Astrophys. J.* **728** (2011) 12.
- [47] R. Geroch, *J. Math. Phys. (N.Y.)* **11**, 1955 (1970).
- [48] R. Geroch, *J. Math. Phys. (N.Y.)* **11**, 2580 (1970).
- [49] R. O. Hansen, *J. Math. Phys. (N.Y.)* **15**, 46 (1974).
- [50] F. D. Ryan, *Phys. Rev. D* **52**, 5707 (1995).
- [51] L. A. Pachón, J. A. Rueda, and J. D. Sanabria-Gómez, *Phys. Rev. D* **73**, 104038 (2006).
- [52] K. Boshkayev, H. Quevedo, and R. Ruffini, *Phys. Rev. D* **86**, 064043 (2012).
- [53] L. A. Pachón, J. A. Rueda, and C. A. Valenzuela-Toledo, *Astrophys. J.* **756**, 82 (2012).
- [54] M. Urbanec, J. C. Miller, and Z. Stuchlík, *Mon. Not. Roy. Astron. Soc.* **433**, 1903 (2013).